

Cite this: DOI: 00.0000/xxxxxxxxxx

# Local structure and lithium ion diffusion pathway of cubic $\text{Li}_7\text{La}_3\text{Zr}_2\text{O}_{12}$ studied by total scattering and the reverse Monte Carlo method

Haolai Tian,<sup>a,b,c</sup> Guanqun Cai,<sup>d</sup> Lei Tan,<sup>d</sup> Anthony E Phillip,<sup>d</sup> Isaac Abrahams,<sup>e</sup> David A Keen,<sup>f</sup> Dean Keeble,<sup>g</sup> Andy Fiedler,<sup>h</sup> Xiang Yang Kong,<sup>h,†</sup> Martin T. Dove,<sup>i,j,‡</sup>

Received Date

Accepted Date

DOI: 00.0000/xxxxxxxxxx

The lithium-bearing oxide  $\text{Li}_7\text{La}_3\text{Zr}_2\text{O}_{12}$  (LLZO), with the cubic garnet crystal structure, is an excellent candidate for solid electrolytes with its structural stability and high  $\text{Li}^+$  conductivity. Here we use neutron and x-ray total scattering methods with the Reverse Monte Carlo method to identify the temperature-dependence of the  $\text{Li}^+$  distribution and of the stability and flexibility of the basic oxide structure. We compare with the results with the outcomes from supporting molecular dynamics simulations. The results give insight into the mechanism of  $\text{Li}^+$  conductivity.

## 1 Introduction

Lithium ion batteries have wide application on electric vehicles, mobile devices, and battery farms for renewable energy storage. However the commonly used liquid-based electrolytes have disadvantages such as flammability, volatile and operating temperature limitations. Although all-solid-state lithium ion batteries (SSLBs) which are expected to enhance the safety reliability and performance issues have been long sought, the conductivity of solid electrolytes can not keep competing at the level of the existed liquid-based counterpart.

Most solid electrolytes require both high  $\text{Li}^+$  conductivity and negligible electronic conductivity. However, in many materials the requirement to match high ionic conductivity with high electrochemical stability for commercialised battery applications is

problematic. Recently the lithium-containing oxide  $\text{Li}_7\text{La}_3\text{Zr}_2\text{O}_{12}$  (LLZO)<sup>1–3</sup>, which crystallises with the cubic garnet structure, has attracted much attention as a potential solid electrolyte because it has both high  $\text{Li}^+$  conductivity and is stable against chemical reaction with Li metal, moisture, air, as well as being able to support both low and high electrical potential differences.

LLZO actually exists in two phases<sup>4</sup>, of cubic and tetragonal symmetry, and the two phases show different  $\text{Li}^+$  conductivities. The conductivity of the cubic phase is two orders of magnitude higher than tetragonal one,  $3 \times 10^{-4}$  S/cm<sup>1</sup> and  $1.63 \times 10^{-6}$  S/cm<sup>5</sup>, respectively. This difference may be related to the distances between Li sites, disorder degree of Li atom, and isotropic diffusion pathways in the cubic phase.

A cubic garnet structure can be described<sup>6</sup> as having a general chemical formula of the form  $\text{A}_3\text{B}_2(\text{TO}_4)_3$ , where the T site has tetrahedral coordination with oxygen (24 sites in the cubic unit cell), the B site has octahedral coordination (16 sites in the unit cell), and the larger A site has 8-fold coordination (24 sites in the unit cell). In LLZO the  $\text{Zr}^{4+}$  cations are in the B sites, and the  $\text{La}^{3+}$  cations are in the A site. The tetrahedral sites are occupied by  $\text{Li}^+$  cations, but full occupancy would only accommodate 3 of the 7 cations of the chemical formula. In crystal structure refinements, sites of general symmetry and irregular coordination with oxygen atoms are associated with the positions of the remaining  $\text{Li}^+$  cations. However, there are 96 of these sites, and therefore there must only be partial occupancy in this model. Indeed, with more than one position available to the  $\text{Li}^+$  cations there is no reason why the tetrahedral sites should be fully occupied, and this partial occupancy is what allows for three-dimensional ionic conductivity.

The atomic structure of LLZO has been studied by two complementary methods. The first is standard crystallography, with

<sup>a</sup> Spallation Neutron Source Science Center, Dongguan 523803, Guangdong, China

<sup>b</sup> Institute of High Energy Physics, Chinese Academy of Sciences, Beijing 100049, China

<sup>c</sup> University of Chinese Academy of Sciences, Beijing 100049, China

<sup>d</sup> School of Physics and Astronomy, Queen Mary University of London, Mile End Road, London, E1 4NS, United Kingdom

<sup>e</sup> School of Biological and Chemical Sciences, Queen Mary University of London, Mile End Road, London, E1 4NS, United Kingdom

<sup>f</sup> ISIS Neutron and Muon Facility, Rutherford Appleton Laboratory, Harwell Campus, Didcot, Oxfordshire, OX11 0QX, United Kingdom

<sup>g</sup> Diamond Light Source Ltd, Harwell Science and Innovation Campus, Didcot, OX11 0DE, United Kingdom

<sup>h</sup> School of Materials Sciences and Engineering, Shanghai Jiao Tong University, Huashan Road 1954, Shanghai 200030, People's Republic of China

<sup>i</sup> College of computer science, Sichuan University, Chengdu, 610065, People's Republic of China

<sup>j</sup> School of Physics, School of Sciences, Wuhan University of Technology, Wuhan, Hubei 430070, People's Republic of China

† Corresponding author: email: xykong@sjtu.edu.cn

‡ Corresponding author: email: martin.dove@icloud.com

both x-ray<sup>4,5,7–11</sup> and neutron<sup>5,7,9,12–15</sup> beams, from which Li<sup>+</sup> sites can be identified and their site occupancies refined. Using a maximum entropy method it was possible to visualise the Li<sup>+</sup> diffusion pathway<sup>13</sup>. The second method is molecular dynamics simulation<sup>15,16</sup>, which has given results broadly consistent with the crystal structure refinements.

In this paper we use the methods of neutron and synchrotron x-ray total scattering methods together with the Reverse Monte Carlo (RMC) method to create an image of the Li<sup>+</sup> site disorder for a wide range of temperatures. The X-ray data are sensitive to the atomic numbers, which means that the data for x-ray total scattering will be mostly sensitive to the La<sup>3+</sup> and Zr<sup>4+</sup> cations, and to a lesser extent to the O<sup>2–</sup> anions, but will have virtually no sensitivity to the Li<sup>+</sup> cations. On the other hand, neutron total scattering will have enhanced sensitivity to the O<sup>2–</sup> anions and, but to a lesser extent also, to the Li<sup>+</sup> cations. The combination of the two techniques will give greater chance to identify the spatial distribution of the Li<sup>+</sup> cations.

## 2 Experimental methods

### 2.1 Synthesis

The precursor materials used was anhydrous LiOH (Alfa Aesar 99.5%, dried at 200 °C overnight; 10 wt.% excess was taken to compensate for the loss of lithium under annealing conditions), La<sub>2</sub>O<sub>3</sub> (Alfa Aesar, treated at 950 °C overnight), ZrO<sub>2</sub> (Alfa Aesar, 99.7%). The reactants were mixed with a mortar and pestle before reacting them at 950 °C for 12 hours. The resultant product was reground and pressed into pellets. The pellets were transferred to an alumina crucible and buried with mother powder, followed by sintering at 1140 °C for 20 hours to form single-phase material. The resulting pellets were grounded into powder and stored in an argon-filled glovebox (<0.1 ppm O<sub>2</sub>, <0.1 ppm H<sub>2</sub>O) to prevent reaction with humidity.

### 2.2 Electrochemical impedance measurements

Electrochemical experiments were carried out in an Ar glovebox (O<sub>2</sub>; H<sub>2</sub>O < 1 ppm). For the electrical measurement, gold electrodes were evaporated on LLZO by thermal evaporation. The EIS was recorded by a Solartron ModuLab system, and contacted via a probe station on a hot stage in the glovebox. EIS was performed with an 10 mV amplitude voltage in a frequency range of 50 mHz to 1 MHz.

### 2.3 Neutron Powder diffraction and total scattering

Neutron powder diffraction and total scattering data were obtained at a number of temperatures on the GEM diffractometer<sup>17</sup> at the ISIS spallation neutron source, Rutherford Appleton Laboratory, UK. The LLZO sample was contained in a cylindrical thin-walled vanadium can of 8 mm diameter. This was mounted in a standard vanadium-foil furnace for measurements at and above room temperature (at 293 K, 450 K, 600 K, 750 K, 900 K and 1100 K). Data were collected on six separate occasions, counting for between 5 and 6 hours per temperature.

Measurements were also performed on the empty instrument, the empty furnace, and an empty vanadium can within the

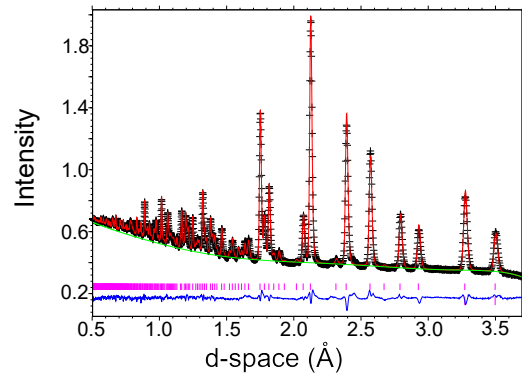


**Fig. 1** Example of the quality of the Rietveld refinement of the crystal structure of LLZO from data collected from the 60° (Bank 4) at temperature of 1100K.

furnace to account for experimental background scattering and sources of beam attenuation, and also of an 8 mm diameter vanadium rod for normalisation. The data were processed using the GudrunN software<sup>18</sup> to obtain the scattering data and pair distribution function as described below, with a maximum scattering vector of  $Q_{\max}$  of 50 Å<sup>-1</sup>. Diffraction data were also corrected and reduced using the Mantid software<sup>19</sup>. Rietveld refinement of the crystal structures was performed by GSAS software<sup>20</sup> with the EXPGUI interface<sup>21</sup>.

### 2.4 Synchrotron total scattering

Synchrotron powder diffraction and total scattering data were collected on the XPDF beamline (I15-1 instrument) at Diamond Light Source (UK). The X-rays were monochromatized to give a wavelength of 0.161669 Å. The sample was sealed into borosilicate capillary tubes (ϕ 1 mm, and 50 mm in length) for measurements at the same temperatures as the neutron beam measurements. The raw data were corrected and reduced into scattering data using the program DAWN<sup>22</sup>. And PDF  $D(r)$  were processed from scattering data using GudrunX<sup>18,23</sup> with the range of data between  $0.5 \leq Q \leq 25$  Å<sup>-1</sup> for the Fourier transformation. Corrections for fluorescence were applied, in which the fluorescence energy of La was assumed to be 38.739 keV.

### 2.5 Pair distribution function from total scattering data

The differential cross section for the scattering of a beam of radiation as integrated over all changes of energy is defined as

$$\frac{1}{N} \frac{d\sigma}{d\Omega} = I(Q) = I^S(Q) + i(Q) \quad (1)$$

where  $I^S(Q) = \sum_m c_m f_m^2$  is the self-scattering of all atoms,  $c_m$  is the fractional amount of atom type  $m$  such that  $\sum_m c_m = 1$ , and  $f_m$  is the scattering factor of atom of type  $m$  (the symbol  $b_m$  is usually used for neutron scattering, denoting the scattering length whose value is independent of  $Q$ )<sup>24</sup>. The function  $i(Q)$  is the total scattering structure factor. Here we define the partial pair distribution function (PDF)  $g_{mn}(r)$  to represent the number of atoms of type  $n$

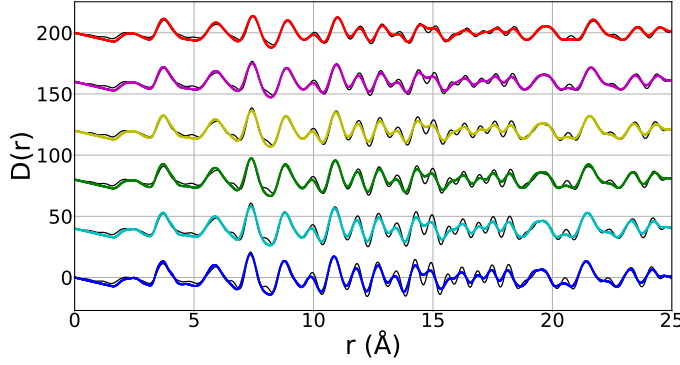


**Fig. 2** Synchrotron pair distribution  $D(r)$  obtained from GudrunX for all temperatures represented as circles. A constant offset has been applied to separate those curves. And RMC modelling are represented by the solid black lines.

within the shell between  $r$  and  $r + dr$  centred on a particle of type  $m$ , namely of value  $4\pi r^2 dr \times c_n \rho \times g_{mn}(r)$ , where  $\rho$  is the overall atomic number density. The structure factor  $i(Q)$  can then be written as<sup>25</sup>

$$i(Q) = 4\pi\rho \int_0^\infty c_m c_n f_m f_n r^2 [g_{mn}(r) - 1] \frac{\sin Qr}{Qr} dr \quad (2)$$

The overall pair distribution function is defined as

$$D(r) = 4\pi\rho r \sum_{m,n} c_m c_n f_m f_n [g_{mn}(r) - 1] \quad (3)$$

so that

$$Qi(Q) = \int_0^\infty D(r) \sin Qr dr \quad (4)$$

In turn, the function  $D(r)$  can be obtained as the sine Fourier transform of  $Qi(Q)$ , but in practice the transform is modified as

$$D(r) = \frac{2}{\pi} \int_0^{Q_{\max}} M(Q) Qi(Q) \sin Qr dr \quad (5)$$

where  $M(Q) = \sin(\pi Q/Q_{\max})/(\pi Q/Q_{\max})$  is the Lorch function, which is introduced to reduce the effect of finite maximum momentum transfer,  $Q_{\max}$ <sup>25–27</sup>. Those tasks were carried out using the programs GudrunX and GudrunN<sup>18,23</sup>.

The PDFs  $D(r)$  for both synchrotron and x-ray total scattering data are shown in Figures 2 and 3 respectively.

## 2.6 Reverse Monte Carlo analysis

The Reverse Monte Carlo (RMC) method, whilst initially developed for the study of highly-disordered (non-crystalline) materials<sup>28</sup>, is in fact an excellent technique for the study of disordered crystalline materials<sup>29</sup>. That said, it appears that there have been only limited applications of the RMC method to crystalline fast-ion conductors<sup>30–33</sup>, and apparently not to the cases where lithium is the mobile ion. We will comment later on some observations on the application of the RMC method to lithium fast-ion conductors in the light of the experience gained in this study.

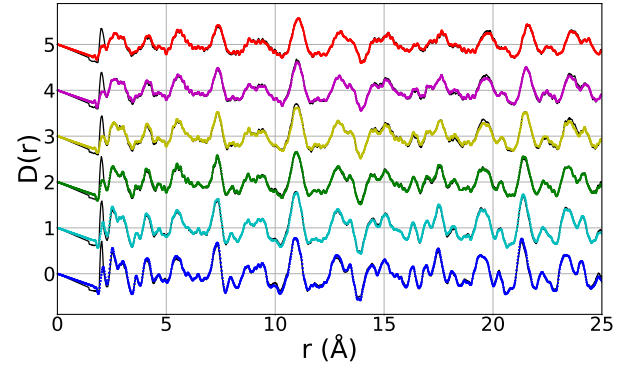


**Fig. 3** Neutron pair distribution  $D(r)$  obtained from GudrunN for all temperatures represented as circles. A constant offset has been applied to separate those curves. The solid black lines indicate the RMC modelling.

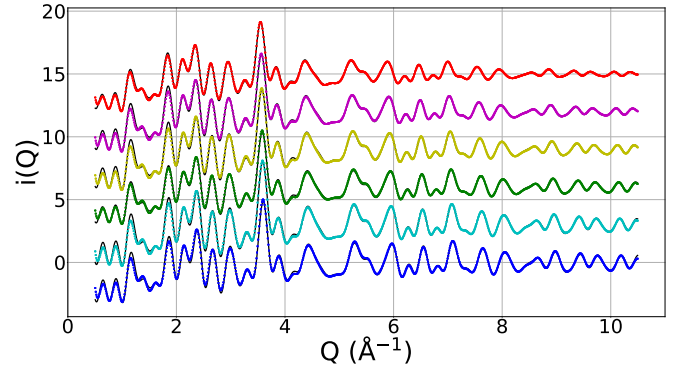


**Fig. 4** Synchrotron scattering function  $i(Q)$  for all temperatures. A constant offset has been applied to separate those curves. In each case the data are shown as circles, and RMC modelling are represented by the solid black lines.

The RMC method is a way to visualise the atomic-scale structure of a material through a simulation based on experimental data. It uses a Monte Carlo method to minimise the difference between experimental functions and the values computed from the atomic configuration as expressed in the function

$$\chi^2 = \sum_j \sum_i (y_{i,j}^{\text{obs}} - y_{i,j}^{\text{calc}})^2 / \sigma_j^2 \quad (6)$$

where  $y_{i,j}^{\text{obs}}$  is the observed values at data point  $i$  in data set  $j$ ,  $y_{i,j}^{\text{calc}}$  is the calculated counterpart, and  $\sigma_j^2$  is weighing function that may represent the statistical accuracy of data set. In this study, the data sets used include  $i(Q)$  from both neutron and synchrotron power diffraction,  $D(r)$  from the neutron total scattering data, and the Bragg data from the neutron diffraction measurements. In the RMC method an selected at random is moved by a random amount up to a specified maximum. The move is accepted if the value of  $\chi^2$  is lowered. On the other hand, if the value of  $\chi^2$  increases by an amount  $\Delta\chi^2$ , the move is accepted only with probability  $\exp(-\Delta\chi^2/2)$ . Each simulation ran until the value of  $\chi^2$  had reached a stable minimum value, corresponding

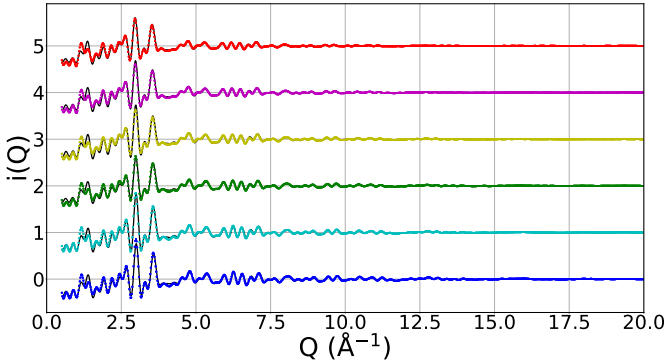


**Fig. 5** Neutron scattering function  $i(Q)$  for all temperatures. A constant offset has been applied to separate those curves. In each case the data are shown as circles, and RMC modelling are represented by the solid black lines.

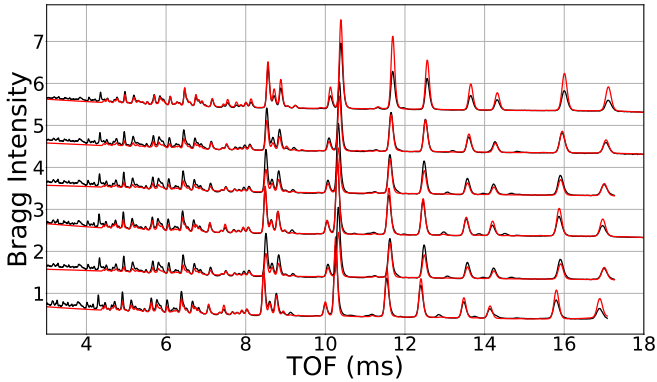


**Fig. 6** The Bragg diffraction data. The data are represented as circles with constant offset to separate those curves. The solid black lines indicate the calculated intensities from GSAS, and RMC modelling are represented by the solid red lines.

in this case to around 300 accepted moves per atom.

The RMC simulations were performed using the program `RMCprofile v6.7`<sup>34</sup>. The starting configurations of  $\text{Li}_7\text{La}_2\text{Zr}_3\text{O}_{12}$  were generated from the results of Rietveld refinement using the `data2config/RMCcreate` program<sup>35</sup>. Configurations were  $4 \times 4 \times 4$  supercell of the conventional body-centred unit cell with linear dimension of around 52 Å, containing 12288 atoms. Maximum atomic moves of La, O and Zr atoms were of size 0.05, but those of Li were 0.1. Minimum distance constraints were applied within the RMC simulation; between pairs of atoms as given in Table 1. Finally, bond-stretching and bond-bending potentials were applied within the  $\text{ZrO}_6$  octahedra, and for the La–O bonds, during the RMC simulation.

It is important to note the contrast between the x-ray and neutron total scattering data. The key point in the formalism, for example equations 2 and 3, is the factor  $c_m c_n f_m f_n$ . The relative sizes of these factors for different atom pairs are compared for both x-ray and neutron scattering in Figure 7. In the case of x-ray scattering, the dominant contribution is for La–La pairs, but all pairs excluding cases with Li as one ion are reasonably strong.

**Table 1** The minimum distances between pairs of atoms

	Li	O	Zr	La
Li	1.69	1.50	2.3	2.3
O		2.2	1.79	2.2
Zr			5.0	3.3
La				3.3

The relative contribution of O–O pairs comes from the fact that is 4 times as many oxygen as Lanthanum giving a relative factor of 16 for  $c_O^2$  over  $c_{\text{La}}^2$ . In spite of the high composition of lithium, the low atomic number still means that none of the pairs containing lithium is significant. Thus the x-ray data will primarily contain information about the heavy metal cations and the oxygen anions. On the other hand, the dominant pair in the neutron scattering is the O–O pair. The other significant pairs are for metal cations and oxygen atoms, this time including the Li–O pair. The pairs involving two metal cations are rather less significant. This shows the complementarity of the synchrotron x-ray and neutron total scattering data. The x-ray data provide information about the network of the heavy cations (La and Zr) and oxygen, and the neutron data provide more weight to the oxygen atom and gives sensitivity to the Li–O pair. What is important to note is that there is very weak sensitivity to Li–Li pairs in *both* synchrotron x-ray and neutron total scattering data. This is despite the relatively high concentration of lithium in this compound,  $c_{\text{Li}} = 7/24 = 0.29$ . This means that we might expect to be able to obtain good information about the structure of the  $\text{La}_2\text{Zr}_3\text{O}_{12}$  network and its fluctuations, and about the density of the Li ions within the channels in the network, but we are unlikely to be unable to obtain robust information on the Li–Li correlations. This is likely to be usually the case in similar studies any any Li-conducting materials.

The fitted PDF functions  $D(r)$  are shown in Figures 2 and 3 for the synchrotron and neutron total scattering data respectively. The corresponding fits to the functions  $i(Q)$  are shown in Figures 4 and 5. The fitted Bragg scattering profiles are shown in Figure 6, where we compare both the Rietveld and RMC calculation profiles with the experimental data.

## 2.7 Molecular dynamics simulation

Classical molecular dynamics (MD) simulations were performed using the `DL_POLY` package<sup>36</sup>. Empirical force-fields were used, which include the long-range Coulomb potential, short-range Buckingham potential functions to describe the energy between two ions of type  $m$  and  $n$ ,  $E_{mn}(r)$ , assumed to be functions of inter-ionic separation  $r$  only:

$$E_{mn}(r) = \frac{Q_m Q_n}{4\pi\epsilon_0 r} + A_{mn} \exp(-r/\rho_{mn}) - C_{mn} r^{-6} \quad (7)$$

with ions treated as rigid entities with no induced polarisation, and assigned formal charges,  $Q_{\text{Zr}} = +4e$ ,  $Q_{\text{La}} = +4e$ ,  $Q_{\text{Li}} = +e$ ,  $Q_{\text{O}} = -2e$ , where  $e$  is the positive unit charge value. The parameters of the force-field were taken from the work of Wang et al<sup>15</sup>, who used a combination of literature and new values; the parameters of the force field are given in Table 2. The starting

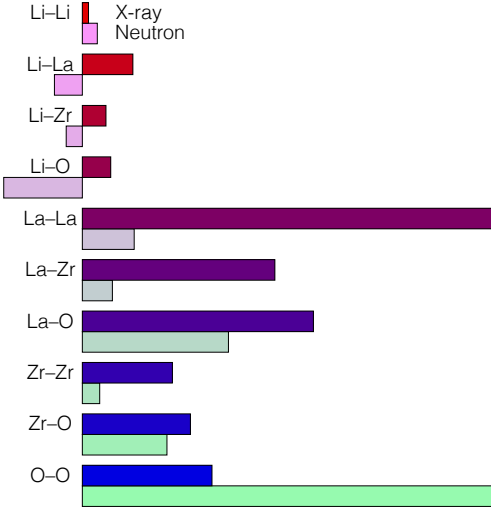


**Fig. 7** Comparison of the relative sizes of the functions  $c_m c_n f_m f_n$  in equations 2 and 3 for all atoms pairs for both x-ray (top bar for each pair) and neutron (bottom bar for each pair) total scattering. Both are normalised against the largest value in each case (there is no direct comparison between the values for the two radiation types). Note that Li has a negative neutron scattering factor. In the case of x-ray scattering, the dominant terms are those where the two atoms are heavy (i.e. not lithium) atoms. In the case of neutron scattering, the dominant terms are for the metal–oxygen pairs, this time including the lithium. What is clear is that in spite the large fraction of lithium atoms in the chemical formula, the contribution from the Li–Li pairs is small in both cases.

**Table 2** Force-field parameters for the molecular dynamics simulations, from the work of Wang et al<sup>15</sup>, with interactions between cations assumed to be give only by the Coulomb interaction. Ions are assigned their formal charge values. The parameters are defined by equation 7.

	A (eV)	$\rho$ ( $\text{\AA}$ )	C ( $\text{eV} \text{\AA}^6$ )
Zr–O	1385.02	1.79	0
La–O	4579.23	0.3044	0
Li–O	632.102	0.2906	0
O–O	22764.30	0.1490	27.63

configurations were the same as used in the RMC work (linear dimensions of around 52 Å, and 12288 atoms), and simulations were performed at the same temperatures as in the neutron and x-ray total scattering measurements.

Simulations were performed within thermodynamic ensembles that were either constant-stress<sup>37,38</sup> and constant temperature<sup>39,40</sup>, or the standard constant-volume constant-energy microcanonical conditions. Simulations were performed using a time step of 0.001 ps, allowing 5 ps for equilibration.

## 3 Results

### 3.1 Ionic conductivity

#### 3.1.1 Electrochemical impedance spectroscopy

The EIS of the LLZO were examined with a in-plane geometry at elevated temperatures from -20°C to 100°C, as shown in Fig.8. From the Nyquist plots, a typical semi arc with the straight tail indicates the ion in-plane diffusion at low frequency occurs along the LLZO. The ion conductivity is about  $2.1 \times 10^{-4}$  S/cm at room

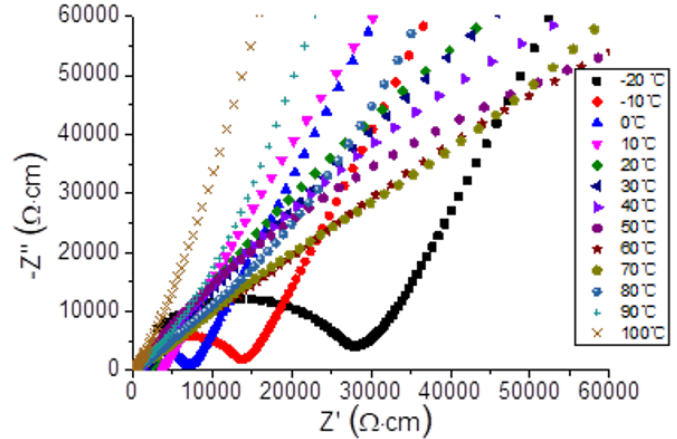


**Fig. 8** AC impedance data collected from -20°C to 100°C.

temperature.

The activation energy can be calculated from the series of EIS at elevated temperatures shown in Fig.9 (top). The activation energy  $E_a$  is estimated based on the Arrhenius equation for the ionic conductivity

$$\sigma T = \sigma_0 e^{-E_a/k_B T} \quad (8)$$

where  $\sigma$  is the ionic conductivity,  $\sigma_0$  is a pre-exponential factor,  $T$  is the absolute temperature, and  $k_B$  is the Boltzmann constant. Furthermore, the diffusion coefficient was calculated using the Nernst-Einstein-equation

$$D = \frac{\sigma k_B T}{N_{Li} q^2} \quad (9)$$

where  $q$  is the charge of the lithium and  $N_{Li}$  the concentration of lithium, in this case for a cubic LLZO structure. The calculated activation energy is about 0.36 eV which is in good agreement to other publications, as well as the diffusion coefficient shown in Fig.9 (bottom) with  $1.31 \times 10^{-13} \text{ m}^2\text{s}^{-1}$  at room temperature.

#### 3.1.2 Lithium-ion diffusion studied by molecular dynamics simulations

The mean square displacement of lithium ions over the temperature range 300–1100 K are shown in Figure 10.

### 3.2 Crystal structure analysis

The structural parameters of LLZO obtained from Rietveld refinement of the neutron scattering data for all temperatures are listed in Table 3 and 4. We refined in the standard space group of  $Ia\bar{3}d$  with two partially-occupied sites for the Li cations suggested by earlier authors<sup>4,5,7–15</sup>. The model gave a good fit to the data, and the example of the fit to the data at 1100 K is shown in Fig. 1. Aspects of this crystal structure have been discussed in the cited previous works; our aim in this paper is to better explore the continuous distribution of Li cation positions and fluctuations in the crystal structure. However, we will remark that the refinement of the two sites for the Li cations

The lattice parameters are plotted as functions of temperature

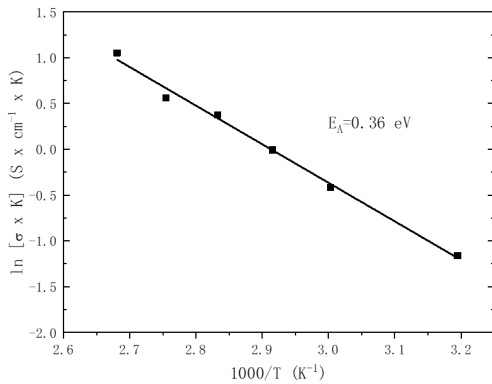


**Fig. 9** Top: Conductivity as a function of temperature for LLZO. The line indicates an Arrhenius fit over the whole temperature range. Bottom: Diffusion coefficient at different temperatures

in Fig. 11, showing a linear thermal expansion. The coefficient of volumetric thermal expansion is  $\alpha_V = 11.8 \times 10^{-6} \text{ K}^{-1}$ .

### 3.3 Local structure analysis

#### 3.3.1 Behaviour of the $\text{La}_2\text{Zr}_3\text{O}_{12}$ network

Some of the partial PDF functions  $g_{mn}(r)$  are shown in Figure 12, comparing the results from both MD and RMC.

The distributions of the Zr–O and La–O bond lengths from both RMC and MD simulations at each temperature are shown in Figure 13. The results from the two methods are, unsurprisingly, consistent in terms of mean distances and the variation of the widths of the distances.

One very interesting feature from both the RMC and MD (actually more strongly seen in the latter) is that the distribution of La–O distances is not symmetric but shows a wider spread to larger distances. This suggests quite a strong anharmonicity, and reflects a similar situation seen in  $\text{CsPbI}_3$  albeit to a lesser extent. In the crystal structure there are two distinct La–O bond lengths (2.53 and 2.63 Å at temperature of 1100 K), but these are not sufficiently different to explain the width of the distribution.

The distributions of O–Zr–O and O–La–O bond angles from both RMC and MD at the different temperatures are shown in Figure 14. The RMC and MD results are consistent in most respects.

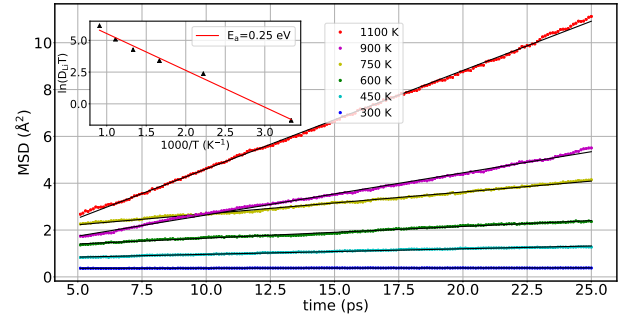


**Fig. 10** Mean squared displacement (MSD) of Li from 300 K to 1100 K. The slope of MSD of each temperature data set yields the diffusion constant (D). The inset shows a diffusion constant (D) versus temperatures.

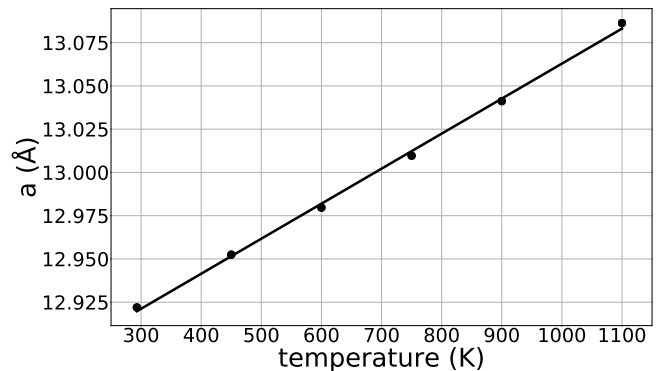


**Fig. 11** Variation of the lattice parameter of  $\text{Li}_7\text{La}_2\text{Zr}_3\text{O}_{12}$  with temperature as obtained by Rietveld analysis (Table 3).

The key features in the O–Zr–O distribution reflect a slightly distorted octahedron, with nearly right-angle bond angles deviating from the ideal 90° by a few degrees. The fluctuations in the O–Zr–O bond angles are slightly larger in the RMC than in the MD, and there are features to indicate a few large distortions of around 20°.

The  $\text{LaO}_8$  polyhedron is not of regular shape. There are two distinct La–O distances in the average structure as noted above, and of the 28 O–La–O bond angles there are 10 distinct angle values which may correspond to 2 or 4 angles. Thus this distribution of O–La–O angles is rather more complicated than for the angles within the  $\text{ZrO}_6$  octahedra, as seen in Figure 14. The MD and RMC both capture this distribution, with the peaks in the distribution from the RMC simulation being slightly broader than from the MD simulation. There is again evidence for some defects in the RMC simulation, with the small peak around 50–60°.

The data for bond lengths and angles (Figures 13 and 14 respectively) show that the  $\text{ZrO}_6$  and  $\text{LaO}_8$  polyhedra retain their integrity across the full range of temperatures in both RMC and MD (aside from some defects in the RMC), with only a slight broadening with increasing temperature. Thus we conclude that the backbone network structure with channels for Li-ion diffusion will remain steady across the whole temperature range.

**Table 3** Lattice parameters, atomic fractional coordinates and Li<sub>2</sub> site occupancy of Li<sub>7</sub>La<sub>2</sub>Zr<sub>3</sub>O<sub>12</sub> obtained from Rietveld refinement. Zr has fractional coordinates 0,0,0, La has fractional coordinates 1/4,0,1/4, Li<sub>1</sub> has fractional coordinates 3/8,0,1/4, and Li<sub>2</sub> has fractional coordinates 1/4,y,z. Note that the Li<sub>1</sub> site occupancy is constrained from the value of that of the Li<sub>2</sub> site as described in the text. Standard deviations are given for the last significant figures in brackets.

T (K)	a (Å)	O x	O y	O z	Li <sub>2</sub> y	Li <sub>2</sub> z	Li <sub>2</sub> occ.
273	12.9219(1)	0.1021(1)	0.1970(1)	0.28162(9)	0.1763(5)	0.4263(5)	0.507(4)
450	12.95247(9)	0.10210(8)	0.19666(8)	0.28141(7)	0.1761(2)	0.4261(2)	0.524(3)
600	12.97967(9)	0.10210(8)	0.19717(8)	0.28136(7)	0.1774(3)	0.4274(3)	0.524(4)
750	13.00096(2)	0.1019(1)	0.19686(9)	0.28123(8)	0.1754(4)	0.4254(4)	0.537(4)
900	13.04123(9)	0.10235(8)	0.19751(8)	0.28060(7)	0.1766(3)	0.4266(3)	0.540(3)
1100	13.08634(8)	0.10184(7)	0.19742(6)	0.28081(6)	0.1772(2)	0.4272(2)	0.504(4)

**Table 4** Atomic displacement parameters,  $100 \times U_{ij}(\text{Å}^2)$ , obtained from Rietveld refinement. For Li<sub>2</sub>  $U_{22} = U_{33}$  and  $U_{12} = -U_{13}$ . Standard deviations are given for the last significant figures in brackets.

T (K)	Li <sub>1</sub> $U_{\text{iso}}$	Li <sub>2</sub> $U_{11}$	Li <sub>2</sub> $U_{22}$	Li <sub>2</sub> $U_{12}$	Li <sub>2</sub> $U_{23}$	O $U_{\text{iso}}$	La $U_{\text{iso}}$	Zr $U_{\text{iso}}$
273	0.9(5)	10(1)	0.19(3)	-3.6(5)	-1.4(3)	0.97(2)	0.63(2)	0.62(3)
450	-0.6(2)	13(1)	0.2(2)	-6.1(4)	-2.5(2)	0.97(1)	0.56(2)	0.35(2)
600	1.4(8)	14(1)	0.5(2)	-4.4(4)	-2.3(3)	1.7(1)	1.16(2)	1.03(3)
750	-2.8(2)	19(1)	1.9(5)	-10.7(8)	-4.9(5)	-0.20(1)	-0.01(2)	-0.43(2)
900	-2.7(1)	16(1)	0.4(3)	-7.4(5)	-3.1(3)	0.74(1)	0.38(2)	-0.10(2)
1100	3.7(7)	16(1)	-0.6(2)	-5.4(4)	-2.9(2)	1.97(1)	1.39(2)	0.93(2)

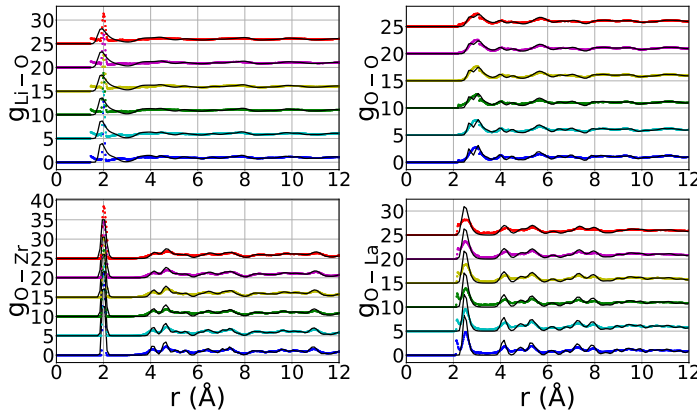


**Fig. 12** The distributions calculated from RMCProfile of (1) Li–O, (2) O–O, (3) Zr–O, and (4) La–O at low- $r$ , show for all temperatures. A constant offset has been applied to separate those curves. In each case the RMC modelling are shown as circles, and the solid black lines indicate the values obtained from Molecular Dynamic simulation

### 3.4 Distribution of lithium cations

By collapsing the configurations down into one unit cell, and drawing only the lithium ions, we can get a feel for the transition pathways. Examples from both RMC and MD (temperature of 273 K) are shown in Figure 15. The two simulations are consistent with each other, except that there is a broader distribution of atoms positions in the RMC. What is clear from the images is that the pathways for the diffusion of lithium ions is not a set of straight lines but a more complex set of connected curves. The three-dimensional connections between separate pathways is clear, but what is apparent is that a simple slice of three-dimensional space will not capture much of the overall picture.

We also remark that simply plotting atoms in a three-

dimensional space is a poor way to represent the quantitative density of atoms. Such a plot, in which points are represented by finite-size spheres, tends to exaggerate the visual representation of the lower-density regions and masks the higher-density regions with many overlapping spheres. In view of the comment regarding the inadequacy of slices of the three-dimensional density, we plot in Figure 16 the projections of the lithium-ion densities onto a surface perpendicular to the crystal 4-fold axes. To reduce statistical noise, not only did we combine six independent configurations in each case but we also applied some of the symmetry operations

The key point seen in Figure 16 is that the lithium ions are clearly not distributed evenly within the channels identified in Figure 15, but have a high probability of being located around a set of identifiable positions. These are the Li<sub>1</sub> and Li<sub>2</sub> positions described in Table 3, as indicated in the top RMC image of Figure 16. What we see in the density plots is that on heating there is a growing density between the special positions, corresponding to increased lithium-ion mobility.

Inspection of Figure 16 shows that the same special places are found for lithium in both the RMC and MD, but their relative weightings are different. Actually, visually the differences in weighting make the RMC and MD results look more different than they really are.

To quantify the results better, we have calculated the density along certain linear directions that contain the Li<sub>1</sub> and Li<sub>2</sub> sites, as indicated by the lines in the MD image at the top. The lithium-ion densities along the linear directions are shown in Figure 17. In both RMC and MD the peaks occur in exactly the same places, and in both cases the peak heights decrease on heating with a broadening that does not commensurably match the decreasing peak eight. This is consistent with the observation of a growing

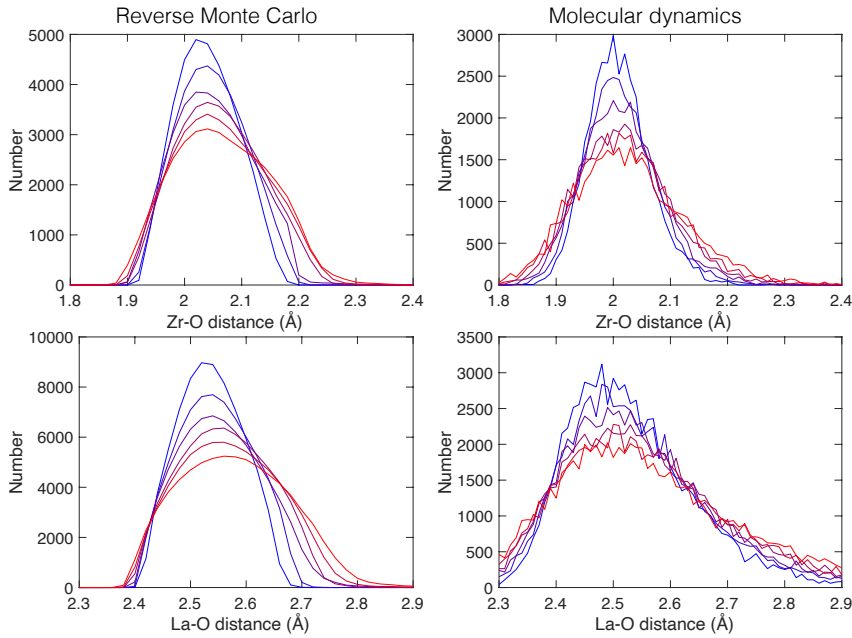


**Fig. 13** The distributions of Zr–O and La–O bond lengths at the different temperatures (blue to red corresponds to 293 K to 1100 K) in both the RMC and MD models, each averaged over six independent configurations.

density of lithium ions between these special positions in Figure 16.

### 3.5 Ionic phonon density of states

From the MD simulations we calculated the velocity autocorrelation functions for each atom type. Fourier transform of these functions give power spectra, the combination of which would give the phonon density of states. Here we show the four atoms types separation, displayed in Figure 18.

The data for different temperatures show exactly the same behaviour for oxygen, zirconium and lanthanum. The much heavier mass of the lanthanum atom means that its power spectrum is mostly around the low-frequency part of the spectrum. On the other hand, the oxygen power spectrum is spread across all frequencies up to 40 THz, reflecting stretching vibrations of Z–O and La–O bonds in addition to the lower mass. The zirconium power spectrum is intermediate reflecting the fact that its mass is lower than lanthanum.

The lithium power spectrum is interesting. The other three power spectra go to zero at low frequency, reflecting the normal Debye frequency-squared dependence of the density of states. However, the lithium power spectra do not go to zero at low frequency, reflecting the diffusion. The size of the power spectrum at zero frequency increases with temperature, as would be expected given that diffusion is a thermally-activated process. What is also interesting about the power spectrum is that there is a significant contribution peaking at around 13 THz and extending to 40 THz. Other most of the frequency range, therefore, the lithium ion appears to be vibrating as a bound particle, with the higher frequency reflecting the light mass of the atom compared with the other atoms. The coincidence of the upper frequency in the power spectrum of lithium with that of oxygen suggests that the

bound Li–O pair execute bond-stretching types of vibrations.

## 4 Conclusions

In this paper we have explored the three-dimensional distribution of lithium ions in the fast-ion conductor  $\text{Li}_7\text{La}_3\text{Zr}_2\text{O}_{12}$  using a combination of simulation by the RMC method based on both neutron and x-ray total scattering data, and by the MD method. There is a high-consistency between the two methods, albeit with some differences concerning the distribution of lithium positions. The backbone  $\text{La}_3\text{Zr}_2\text{O}_{12}$  network is robust at all temperatures. The network defines a set of curved pathways for the motions of lithium ions.

The results of the two simulations are supported by ionic conductivity measurements to give the lithium ion diffusion. These results are reproduced by the MD simulations.

The key result of this paper is to explore this diffusion pathway from both experiment and simulation. Here is where there are similarities in both methods but also some differences. In both cases there is a pattern of the lithium ions preferentially lying close to some specific sites and moving between these sites. The changes in occupancy on heating corresponding to the ions moving into the channels. On the other hand, the relative weights of the two types of special site are different between the RMC and MD.

## 5 Appendix

### 5.1 The correlation functions

Time-dependent correlation functions are valuable tools to describe the average way the quantity will change with time, and predict the trends within the behaviour of atomic structure and dynamics.

One of the simplest correlation function for velocity with a

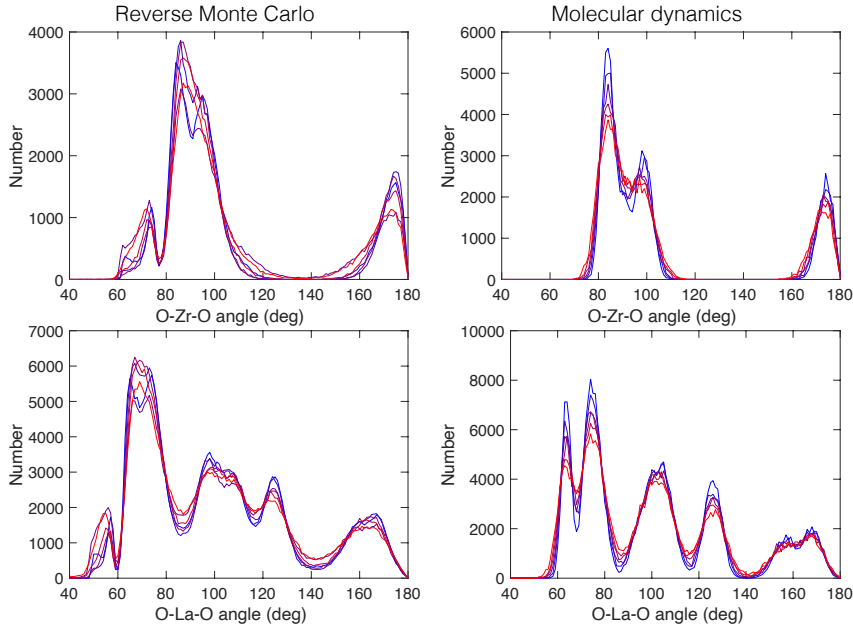


**Fig. 14** The distributions of O–Zr–O and O–La–O bond angles at the different temperatures (blue to red corresponds to 293 K to 1100 K) in both the RMC and MD models, each averaged over six independent configurations.

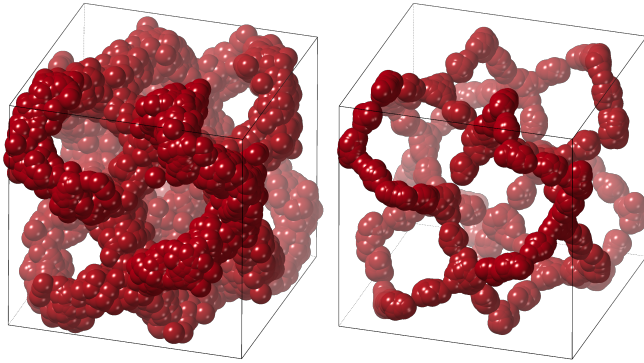


**Fig. 15** Distribution of instantaneous lithium-ion positions in RMC (left) and MD (right) configurations, obtained by collapsing each configuration down to one unit cell and then adding 6 separate configurations.

mean value of zero,  $C(t)$ , is defined as

$$C(t) = \frac{\langle v(0)v(t) \rangle}{\langle |v(0)|^2 \rangle} = \frac{(\lim \mathcal{T} \rightarrow \infty) \frac{1}{\mathcal{T}} \int_0^{\mathcal{T}} v(t')v(t+t')dt'}{\langle v^2 \rangle} \quad (10)$$

For the harmonic crystal, the velocity of the  $j$ -th atom is given as

$$v_j(t) = \frac{-i}{(Nm_j)^{1/2}} \sum_{\mathbf{k},v} \omega(\mathbf{k},v) \mathbf{e}_j(\mathbf{k},v) \exp(i\mathbf{k} \cdot \mathbf{r}) Q(\mathbf{k},v,t) \quad (11)$$

and leads to the classical result:

$$\sum_j m_j \langle |v_j(t) \cdot v_j(0)| \rangle = \frac{k_B T}{N} \sum_{\mathbf{k},v} \cos(\omega(\mathbf{k},v)t) \quad (12)$$

In addition, the power spectra  $Z(\omega)$  is given by the Fourier transform of  $C(t)$ :

$$Z(\omega) = \int C(t) \exp(-i\omega t) dt \quad (13)$$

It can be seen that the power spectrum of the mass-weighted velocity correlation function is equal to the phonon density of states.

Consider another correlation function for position of atom,  $G_s(r,t)$ , is defined as

$$\begin{aligned} G_s(\Delta r, t) &= \frac{\langle r(0)r(t) \rangle}{\langle |r(0)|^2 \rangle} \\ &= \frac{1}{N} \sum_j^N \int \langle \delta(r' - r_j(0)) \delta(r' + \Delta r - r_j(t)) dr' \rangle \\ &= \frac{1}{N} \langle \sum_j^N \delta(\Delta r + r_j(0) - r_j(t)) \rangle \end{aligned}$$

which is related to the probability of finding an atom in the volume  $dr$  at position  $\Delta r$  for a time interval of  $t$ , and can be named as self-part of van Hove correlation function.

The mean square displacement (MSD)  $\langle \Delta r_i(t) \rangle^2$  is a measure of the deviation of the position of an atom with respect to a reference position over time. MSD is related to the  $G_s(r,t)$  as:

$$\langle \Delta r_i(t) \rangle^2 = \int_0^\infty (\Delta r_i(t))^2 \cdot 4\pi (\Delta r_i(t))^2 G_s(\Delta r, t) d\Delta r \quad (14)$$

## 5.2 Nernst-Einstein equation

The value of ionic conductivity ( $\sigma$ ) is determined by the impedance spectroscopy. In solid electrolytes, as the anions are immobile, the ionic conduction is driven by the diffusion of  $\text{Li}^+$  ions. The connection between the diffusion constant (D) and  $\sigma$  is

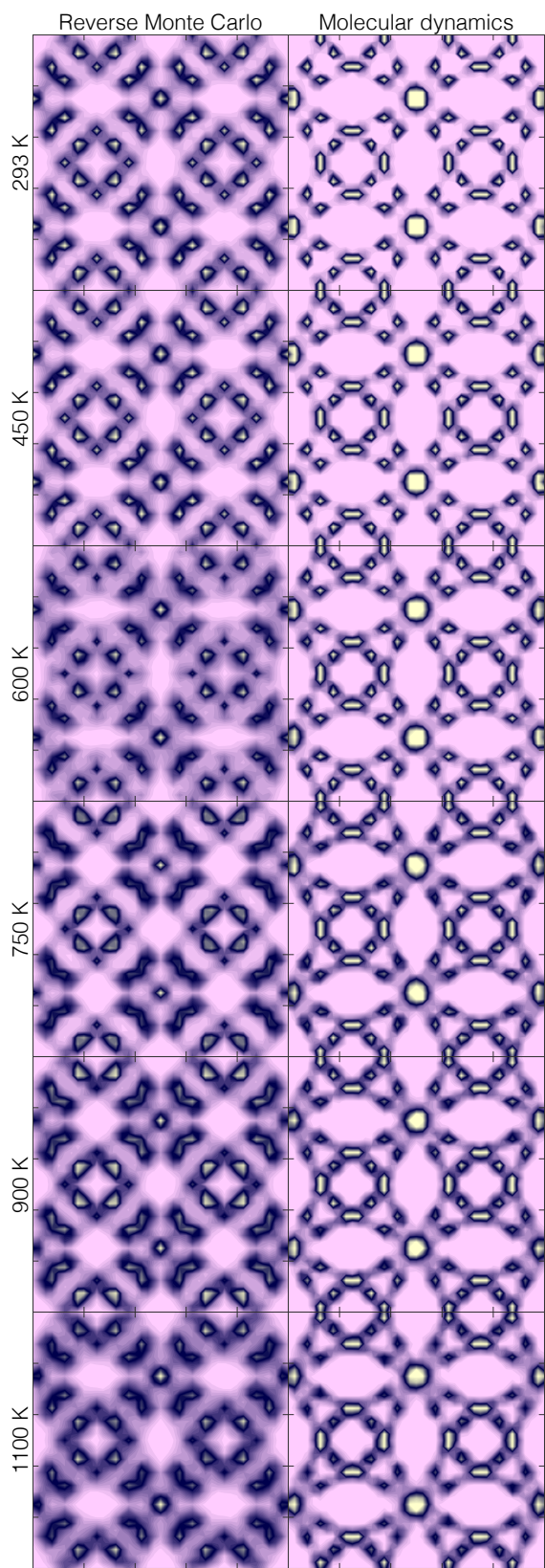


**Fig. 16** Li-density plots.

defined by the Nernst-Einstein (NE) equation, which are widely used for electrolyte system. NE equation is given as

$$D(T) = \frac{kT}{Ne^2} \sigma(T) \quad (15)$$

where  $k$  is the Boltzmann constant,  $e$  is the elementary charge, and  $N$  is the number of carrier ions.

## Conflicts of interest

There are no conflicts to declare.

## Acknowledgements

The Acknowledgements come at the end of an article after Conflicts of interest and before the Notes and references.

## References

- 1 R. Murugan, V. Thangadurai and W. Weppner, *Angewandte Chemie International Edition*, 2007, **46**, 7778–7781.
- 2 A. J. Samson, K. Hofstetter, S. Bag and V. Thangadurai, *Energy & Environmental Science*, 2019, **12**, 2957–2975.
- 3 K. Kataoka, *Journal of the Ceramic Society of Japan*, 2020, **128**, 7–18.
- 4 C. A. Geiger, E. Alekseev, B. Lazic, M. Fisch, T. Armbruster, R. Langner, M. Fechtelkord, N. Kim, T. Pettke and W. Weppner, *Inorganic Chemistry*, 2011, **50**, 1089–1097.
- 5 J. Awaka, N. Kijima, H. Hayakawa and J. Akimoto, *Journal of Solid State Chemistry*, 2009, **182**, 2046–2052.
- 6 E. J. Cussen, T. W. S. Yip, G. O'Neill and M. P. O'Callaghan, *Journal of Solid State Chemistry*, 2011, **184**, 470–475.
- 7 H. Buschmann, J. D o lle, S. Berendts, A. Kuhn, P. Bottke, M. Wilkening, P. Heitjans, A. Senyshyn, H. Ehrenberg, A. Lotnyk, V. Duppel, L. Kienle and J. Janek, *Physical Chemistry Chemical Physics*, 2011, **13**, 19378–15.
- 8 J. Awaka, A. Takashima, K. Kataoka, N. Kijima, Y. Idemoto and J. Akimoto, *Chemistry Letters*, 2011, **40**, 60–62.
- 9 Daniel Rettenwander, G. J. Redhammer, F. Preishuber-Pflugl, L. Cheng, L. Miara, R. Wagner, A. Welzl, E. Suard, Marca M Doeffer, M. Wilkening, J. Fleig and G. Amthauer, *Chemistry of Materials*, 2016, **28**, 2384–2392.
- 10 R. Wagner, G. J. Redhammer, D. Rettenwander, A. Senyshyn, W. Schmidt, M. Wilkening and G. Amthauer, *Chemistry of Materials*, 2016, **28**, 1861–1871.
- 11 K. Kataoka and J. Akimoto, *Journal of the Ceramic Society of Japan*, 2019, **127**, 521–526.
- 12 H. Xie, J. A. Alonso, Y. Li, M. T. Fernamdex-Diaz and J. B. Goodenough, *Chemistry of Materials*, 2011, **23**, 3587–3589.
- 13 J. Han, J. Zhu, Y. Li, X. Yu, S. Wang, G. Wu, H. Xie, S. C. Vogel, F. Izumi, K. Momma, Y. Kawamura, Y. Huang, J. B. Goodenough and Y. Zhao, *Chemical Communications*, 2012, **48**, 9840–3.
- 14 Y. Li, J.-T. Han, C.-A. Wang, S. C. Vogel, H. Xie, M. Xu and J. B. Goodenough, *Journal of Power Sources*, 2012, **209**, 278–281.
- 15 Y. Wang, A. Huq and W. Lai, *Solid State Ionics*, 2014, **255**, 39–49.
- 16 M. Klenk and W. Lai, *Physical Chemistry Chemical Physics*, 2015, **17**, 8758–8768.
- 17 A. C. Hannon, *Nuclear Instruments and Methods in Physics Research*

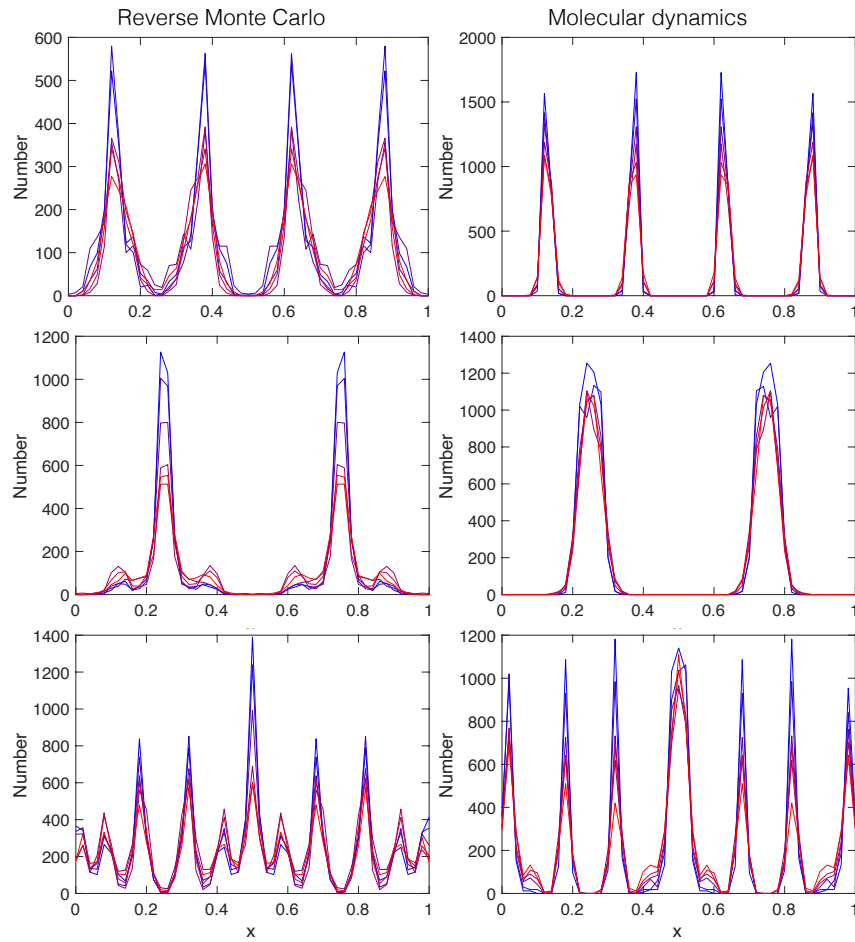


**Fig. 17** Li-density plots.

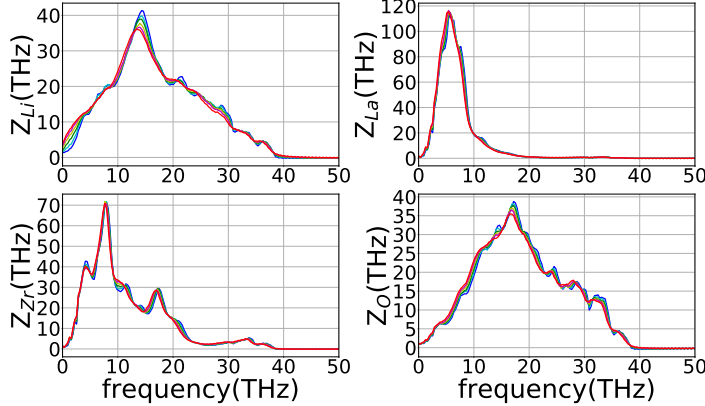


**Fig. 18** The power spectra of (1) Li, (2) La, (3) Zr, (4) O for all temperatures.

- search Section A: Accelerators, Spectrometers, Detectors and Associated Equipment, 2005, **551**, 88–107.
- 18 A. K. Soper, *GudrunN and GudrunX : programs for correcting raw neutron and X-ray diffraction data to differential scattering cross section*, Rutherford Appleton Laboratory Technical Report RAL-TR-2011-013, 2011.

- 19 O. Arnold, J. C. Bilheux, J. M. Borreguero, A. Buts, S. I. Campbell, L. Chapon, M. Doucet, N. Draper, R. F. Leal, M. A. Gigg, V. E. Lynch, A. Markvardsen, D. J. Mikkelson, R. L. Mikkelson, R. Miller, K. Palmen, P. Parker, G. Passos, T. G. Perring, P. F. Peterson, S. Ren, M. A. Reuter, A. T. Savici, J. W. Taylor, R. J. Taylor, R. Tolchenov, W. Zhou and J. Zikovsky, *Nuclear Inst. and Methods in Physics Research, A*, 2014, **764**, 156–166.
- 20 A. C. Larson and R. B. Von Dreele, *General Structure Analysis System (GSAS)*, Los Alamos National Laboratory Technical Report LAUR 86-748, 2004.
- 21 B. H. Toby, *Journal of Applied Crystallography*, 2001, **34**, 210–213.
- 22 M. Basham, J. Filik, M. T. Wharmby, Chang, P.C.Y., B. El Kassaby, M. Gerring, J. Aishima, K. Levik, B. C. A. Pulford, I. Sikharulidze, D. Sneddon, M. Webber, S. S. Dhesi, F. Maccherozzi, O. Svensson, S. Brockhauser, G. Naray and A. W. Ashton, *J. Synchrotron Rad* (2015). **22**, 853–858 [doi:10.1107/S1600577515002283], 2015, 1–6.
- 23 A. K. Soper and E. R. Barney, *J. Appl. Cryst* (2011). **44** [doi:10.1107/S0021889811021455], 2011, 1–13.
- 24 D. A. Keen, *Journal of Applied Crystallography*, 2001, **34**, 172–177.
- 25 M. T. Dove, M. G. Tucker and D. A. Keen, *European Journal of*

- Mineralogy*, 2002, **14**, 331–348.
- 26 E. Lorch, *Journal of Physics C: Solid State Physics*, 1969, **2**, 229–237.
- 27 A. K. Soper and E. R. Barney, *Journal of Applied Crystallography*, 2012, **45**, 1314–1317.
- 28 R. L. McGreevy and L. Pusztai, *Molecular Simulation*, 1988, **1**, 359–367.
- 29 D. A. Keen, M. G. Tucker and M. T. Dove, *Journal of Physics: Condensed Matter*, 2005, **17**, S15–S22.
- 30 S. Adams and J. Swenson, *Physical Review Letters*, 2000, **84**, 4144–4147.
- 31 J. Swenson and S. Adams, *Physical Review B*, 2001, **64**, 281–10.
- 32 S. Adams, *Solid State Ionics*, 2002, **154-155**, 151–159.
- 33 S. Adams and J. Swenson, *Journal of Physics: Condensed Matter*, 2005, **17**, S87–S101.
- 34 M. G. Tucker, D. A. Keen, M. T. Dove, A. L. Goodwin and Q. Hui, *Journal of Physics: Condensed Matter*, 2007, **19**, 335218–16.
- 35 M. T. Dove and G. Rigg, *Journal of Physics: Condensed Matter*, 2013, **25**, 454222–9.
- 36 I. T. Todorov, W. Smith, K. Trachenko and M. T. Dove, *Journal of Materials Chemistry*, 2006, **16**, 1911–8.
- 37 M. Parrinello and A. Rahman, *Physical Review Letters*, 1980, **45**, 1196–1199.
- 38 S. Melchionna, G. Ciccotti and B. Lee Holian, *Molecular Physics*, 2006, **78**, 533–544.
- 39 S. Nosé, *The Journal of Chemical Physics*, 1984, **81**, 511–10.
- 40 W. G. Hoover, *Physical Review A*, 1985, **31**, 1695–1697.